ChemElectroChem
Research Article
doi.org/10.1002/celc.202500103
Chemistry Europe
European Chemical Societies Publishing

www.chemelectrochem.org

Metal–Support Interaction Between Titanium Oxynitride and Pd Nanoparticles as a Tool for Tuning the Selectivity of Electrocatalytic Hydrogenation of Furfural

Nik Maselj, Jan Trputec, Martin Šala, Kristina Mervič, Ivan Marić, Francisco Ruiz-Zepeda, Marjan Bele, Vasko Jovanovski, Nejc Hodnik, and Primož Jovanovič*

Electrocatalytic hydrogenation (ECH) offers a sustainable alternative to conventional hydrogenation of biomass-derived compounds by using cathodic potential instead of heat and molecular hydrogen. This study explores the ECH of furfural under acidic conditions, focusing on how metal–support interactions influence the performance of Pd-based catalysts. Two systems are compared: Pd on carbon (Pd/C) and Pd supported on titanium oxynitride-graphene oxide (Pd–TiONx/GO). Pd–TiONx/GO exhibits lower oxophilicity and a higher proton adsorption tendency than Pd/C. Additionally, its surface shows a more negative charge, indicated by a cathodic shift (≈10 mV) in the potential of zero total charge measured via N_2O reduction. These differences significantly affect catalytic behavior. While Pd/C shows roughly twice the activity for converting furfural to furfuryl alcohol (FA), Pd–TiONx/GO is over 100 times more active in producing 2-methylfuran (2-MF) and also enhances the competitive hydrogen evolution reaction. This suggests Pd–TiONx/GO has lower surface coverage by furfural and FA, allowing for more hydrogen adsorption and favouring 2-MF formation. Overall, the study demonstrates that Pd's electrosorptive and catalytic properties can be tuned via electronic effects from the TiONx support, enabling selective manipulation of ECH pathways.

1. Introduction

Lignocellulosic biomass represents the most credible carbon-based source for the production of renewable fuels, chemicals, and chemicals in the near future. Unfortunately, major scientific challenges need to be overcome on the way to the techno-economic realization of biorefineries. Regardless of the type of depolymerization of the biomass, the product matrix consists of a mixture of oxygenate compounds with a high or low O/C ratio. In the first case, the compounds are rather unsuitable for immediate implementation in the chemical industry due to their insufficient energy density and high reactivity. This means that oxidative conversions must be used. On the other hand, compounds with a low O/C ratio (high H/C ratio) can be hydrogenated to energy-dense fuels.[1–3] Here, furfural (FF) is one of the main contenders and is considered one of the most important platform chemicals in the conversion of biomass, which has been established for decades and currently amounts to 400 kt/year.[4–6] It can be produced quite easily from hemicellulose-rich biomass, and its further conversion can lead to a wide range of alternative fuels and value-added chemicals conventionally produced from petroleum-based feedstocks. The most valuable products from the upgrading of FF by hydrogenation are furfuryl alcohol (FA) and 2-methylfuran (2-MF). The former is typically used as a precursor for polymer and resin synthesis, while 2-MF is a promising biofuel additive and potential liquid fuel.[4,7] If electrochemical conversion can be implemented into the FF platform, further techno-economic readiness could be achieved. In particular, electrochemical reactions offer a number of advantages as they ideally run under mild conditions (room temperature and ambient pressure) and can bypass external toxic reagents. Moreover, they can be carried out directly in aqueous solutions, with electrochemical potentials being the driving forces. When powered by renewable energy sources such as wind or solar, this inherently sustainable and "green" approach makes electrons a cost-effective, clean, and energy-efficient reagent.

Indeed, the electrochemical conversion of FF has been of growing interest over the last decade, with a focus on electrochemical hydrogenation (ECH). In aqueous electrolytes, FA and

---

N. Maselj, J. Trputec, F. Ruiz-Zepeda, M. Bele, V. Jovanovski, N. Hodnik, P. Jovanovič
Department of Materials Chemistry
National Institute of Chemistry
Hajdrihova 19, 1000 Ljubljana, Slovenia
E-mail: Primoz.jovanovic@ki.si

N. Maselj, J. Trputec, N. Hodnik
Faculty of Chemistry and Chemical Engineering
University of Ljubljana
Večna pot 113, 1000 Ljubljana, Slovenia

M. Šala, K. Mervič
Department of Analytical Chemistry
National Institute of Chemistry
Hajdrihova 19, 1000 Ljubljana, Slovenia

I. Marić
Radiation Chemistry and Dosimetry Laboratory
Division of Materials Chemistry
Ruđer Bošković Institute
Bijenička cesta 54, 10 000 Zagreb, Croatia

Supporting information for this article is available on the WWW under https://doi.org/10.1002/celc.202500103

2-MF products are predominantly obtained,[8] with the product distribution depending on the type of metal electrode, the pH of the electrolyte, and the FF concentration.[9–12] In particular, three different mechanisms are possible on metal electrodes, namely ECH, proton concerted electron transfer (PCET), and direct electroreduction.[13–15] In regards to the metal selection, copper analogs are the most frequently studied electrocatalysts in which hydrogenation (FA) and hydrogenolysis (2-MF) products are generated in parallel pathways.[13] Notably, at least in the case of Cu, there is no general consensus on the contributions of the individual mechanisms to the observed product distribution. Initially, it was generally assumed that the ECH pathway to both products proceeds via adsorbed hydrogen (H_{ads}), whereas more recent studies suggest that surface hydrogenation via H_{ads} plays only a minor role compared to the PCET steps due to the negligible H_{ads} coverage (θ_H) on Cu.[15,16] However, for metals with high proton adsorption affinity (e.g., Pt, Pd), the H_{ads} pathway prevails over the PCET pathway and thus affects reaction selectivity.[15,17,18] Accordingly, the strategies used to date to improve the ECH activity and selectivity were aimed at manipulating the electronic properties of the catalyst surface by alloying noble and non-noble metals.[19–21] The induced strain and ligand effects have been shown to lead to more optimal adsorption of H and FF by benefiting from more mature branches of electrocatalysis, such as the oxygen reduction reaction.[22–25] Capitalizing on more mature heterogeneous catalysis, another useful strategy is to exploit the synergy between the active Pd sites and the supporting substrate, i.e., the so-called strong metal–support interaction (SMSI), which mediates the catalytic behavior of metal nanoparticles.[26–29] In general, this can occur via one of the following mechanisms. Namely, the formation of an active site when the support decorates the metal particle,[30,31] activation and spillover from a chemically active site in the support,[32] and via electronic mediation through various routes of charge transfer.[33,34] In comparison to heterogeneous catalytic hydrogenation, the use of SMSI in the context of ECH of FF is hardly known. Therefore, here we perform a comparative analysis of how Pd nanoparticles supported on either a carbon support or a titanium oxynitride analog affect ECH.

2. Results and Discussion

Results of the X-ray diffraction (XRD) analysis are given in Figure S1, Supporting Information. The diffraction pattern of Pd-$TiON_x$/GO can be fully characterized by three phases, graphene oxide (marked by a black diamond), titanium oxynitride (ICDD card 04-001-9292), and palladium. The two peaks at 37.04° and 43.04° correspond to 111 and 200 diffraction lines of titanium oxynitride (space group Fm-3 m), while the two peaks at 40.01° and 46.54° correspond to the same 111 and 200 lines of cubic palladium (space group Fm-3 m). As can be seen from the diffraction patterns, the wet-chemical deposition of Pd on $TiON_x$ does not affect the position of the diffraction lines of $TiON_x$, implying no change in the ratio of oxygen to nitrogen in the support. According to scanning electron microscope (SEM) micrographs (see Section S7), $TiON_x$ particles with a typical size of ≈20 nm are observed, and forming coatings that cover the graphene sheets (Figure S6, Supporting Information). The graphene sheets vary in size from a few micrometers to several tens of micrometers. The graphene sheets are in contact with each other, ensuring good interconnections and efficient electronic wiring. Due to their small size, Pd nanoparticles are not visible in the SEM images. According to the energy dispersive x-ray spectroscopy (EDS) analysis, Pd-$TiON_x$/GO consists of 14 wt% of Pd, 35 wt% of Ti, 26 wt% of C, 12 wt% of N, and 12 wt% of O.

Based on scanning transmission electron microscopy (STEM) analysis, the Pd-$TiON_x$/GO composite consists of small Pd particles in the range of ≈3–5 nm, which are predominantly supported on $TiON_x$ crystals (**Figure 1**b). A detailed structural characterization of the Pd/C analog can be found in our recent publication. Briefly, according to STEM imaging Pd/C sample contains uniform-sized Pd nanoparticles, the majority of which have a diameter in the range between 2 and 6 nm (Figure 1a).[44]

Initially, voltammetric responses for the two analogs were pursued, focusing on the fingerprint redox characteristics of Pd. Accordingly, typical profiles for Pd in aqueous acidic solutions are observed for both analogs (**Figure 2**a). Pd oxidation initiates at ≈0.7 V (labeled as A1) in the anodic scan, while a well-resolved PdO reduction peak is seen below 0.8 V (labeled as C1) in the

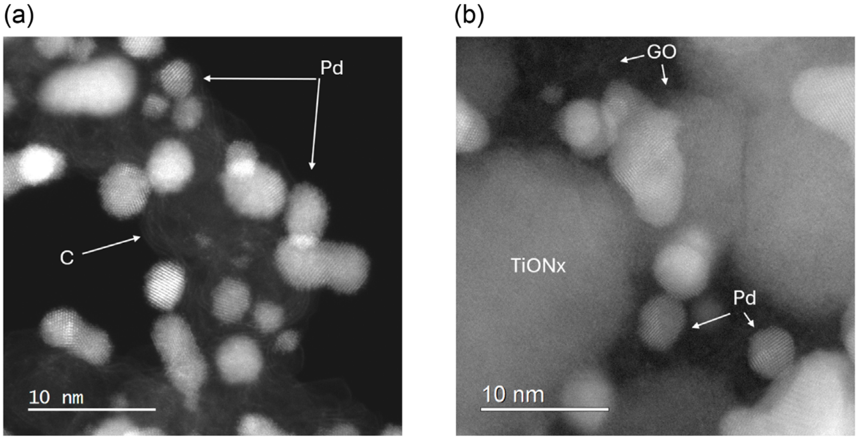

Figure 1. STEM ADF imaging of a) Pd/C and b) Pd/$TiON_x$/GO.

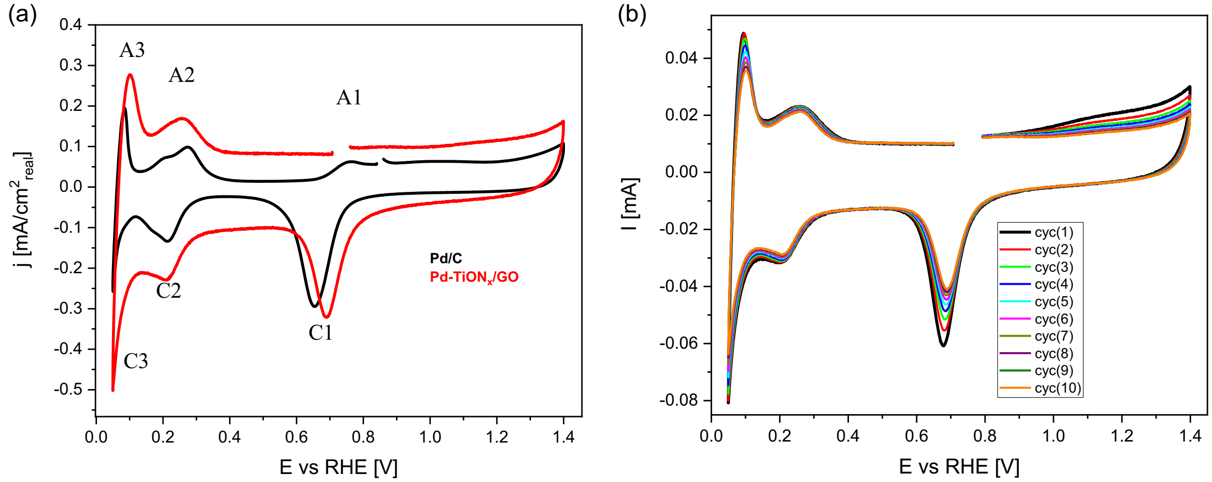

Figure 2. a) Fingerprint voltammogram for Pd-TiON$_x$/GO and Pd/C analogs (50 mV s^{-1}). Current response is normalized per Pd surface area. b) Evolution of fingerprint voltammogram (50 mV s^{-1}) during sequential cycling for the case of Pd-TiON$_x$/GO. Each cycle sequence encompassed 10 cycles (cycy, 300 mV s^{-1}) between 0.05–1.2 V.

cathodic scan, as expected from the extensive literature.[44–51] At low potentials (<0.4 V), the voltammetric profile consists of cathodic and anodic peaks corresponding to the hydrogen under potential deposition (HUPD) adsorption/desorption (peaks A2/C2) and H absorption/desorption i.e., formation of Pd hydride (PdH), respectively (peaks A3/C3).[51–54] From comparative analysis, the most evident voltammetric distinction between the two analogs is the anodic shift (≈40 mV) of the PdO reduction peak for the Pd-TiON$_x$/GO sample, indicating the inherent differences between the two samples. In particular, the shift indicates that more of the thicker (hydrous) oxide is formed in the Pd/C analog[55] with a higher activation barrier for reduction[56] while a larger amount of the compact (thin) oxide should be present in Pd-TiON$_x$/GO.[46,47,55,57,58] Therefore, Pd particles in the former seem to show more oxophilic character. The second notable distinction is the ratio between the HUPD charge (Q_{HUPD}) and the PdO reduction charge ($Q_{PdO}/2$, i.e., normalized per 2e$^-$). For Pd-TiON$_x$/GO, a ratio of ≈1 is obtained in comparison to ≈1.4 for Pd/C, which may fit the postulate of the more oxophilic nature of Pd particles in the latter. Overall, the voltammetric comparison suggests that the electrosorptive properties differ for the two Pd analogs. The altered oxophilicity seems to be due to the oxidative transformation of TiON$_x$/GO support during electrochemical pretreatment, as demonstrated by a gradual anodic shift of the PdO reduction peak with the pretreatment cycles (Figure 2b).

To obtain more insight, we conducted experiments under potentiodynamic perturbations by varying the scan rate, focusing on the trends associated with PdO reduction charge (Q_{PdO}). Interestingly, the two analogs show an opposite trend with either an increase (Pd/C) or a decrease (Pd-TiON$_x$/GO) in Q_{PdO} while varying the scan rate (**Figure 3**a). We note that the Q_{PdO} increases with scan rate is characteristic for the reduction of hydrous oxide,[46,55,57] while the opposite trend is typical for the compact oxides, such as in the case of platinum.[39,59] The discrepancies in the redox behavior are quantitatively compared by the apparent surface coverage analysis ($\theta_{O/OH}$, see Experimental Section for details on its determination). Here, $\theta_{O/OH}$, like with $Q_{PdO,}$ either increases (Pd/C) or decreases (Pd-TiON$_x$/GO) with the scan rate (Figure 3b,c). The obtained trends in Q_{PdO} and $\theta_{O/OH}$ for Pd-TiON$_x$/GO highlight an anomalous behavior of the palladium surface/subsurface, indicating that the Pd–TiON$_x$ interaction inhibits Pd oxidation. An analogous coverage analysis was performed to obtain the coverage with hydrogen (θ_H). Interestingly, in this case, the θ_H is continuously higher for Pd-TiON$_x$/GO within the selected potential window (Figure 3d), giving further credence to the altered electrosorptive properties of the two analogs. However, whether the support-induced change in the Pd character is due to the change in its intrinsic electronic properties or to the chemical modification of the Pd surface is uncertain at this stage.

If an electronic interaction is at play, there should be an effect on the potential of zero charge. However, the only experimentally accessible parameter in this context is the potential of zero total charge (PZTC), the potential at which the free, excess electronic charge plus the charge transferred during adsorption processes equals zero.[60–62] Notably, the surface coverage is the lowest at PZTC, and therefore most accessible for nonspecific adsorbing molecules such as N_2O. In this respect, the N_2O reduction reaction (N_2O-RR) can be exploited as a chemical probe that is sensitive to the PTZC due to its sufficiently weak adsorption[63] that does not alter the adsorption isotherm of the other components at ambient pressure.[64,65] More specifically, assuming competitive adsorption between weakly adsorbing N_2O and other adsorbed species (e.g., HUPD, anions, and water), the reaction rate is highest when the surface coverage is at its minimum. This occurs when the number of available sites for N_2O adsorption is the largest, i.e., at the PZTC.[65] N_2O-RR polarization curves for Pd/C and Pd-TiON$_x$/GO analogs are shown in **Figure 4**a. Notably, the potential at the observed maximum current (i.e., PZTC) is cathodically shifted (≈10 mV) for Pd-TiON$_x$/GO, indicating a more negatively charged Pd surface. Interestingly, there are large differences present in terms of surface area normalized N_2O-RR performance ($j_{N2O\text{-}RR}$), where the Pd-TiON$_x$/GO analog shows much lower activity. Note that the N_2O-RR response is normalized to the real Pd surface area, which is justified by the fact that the reaction is

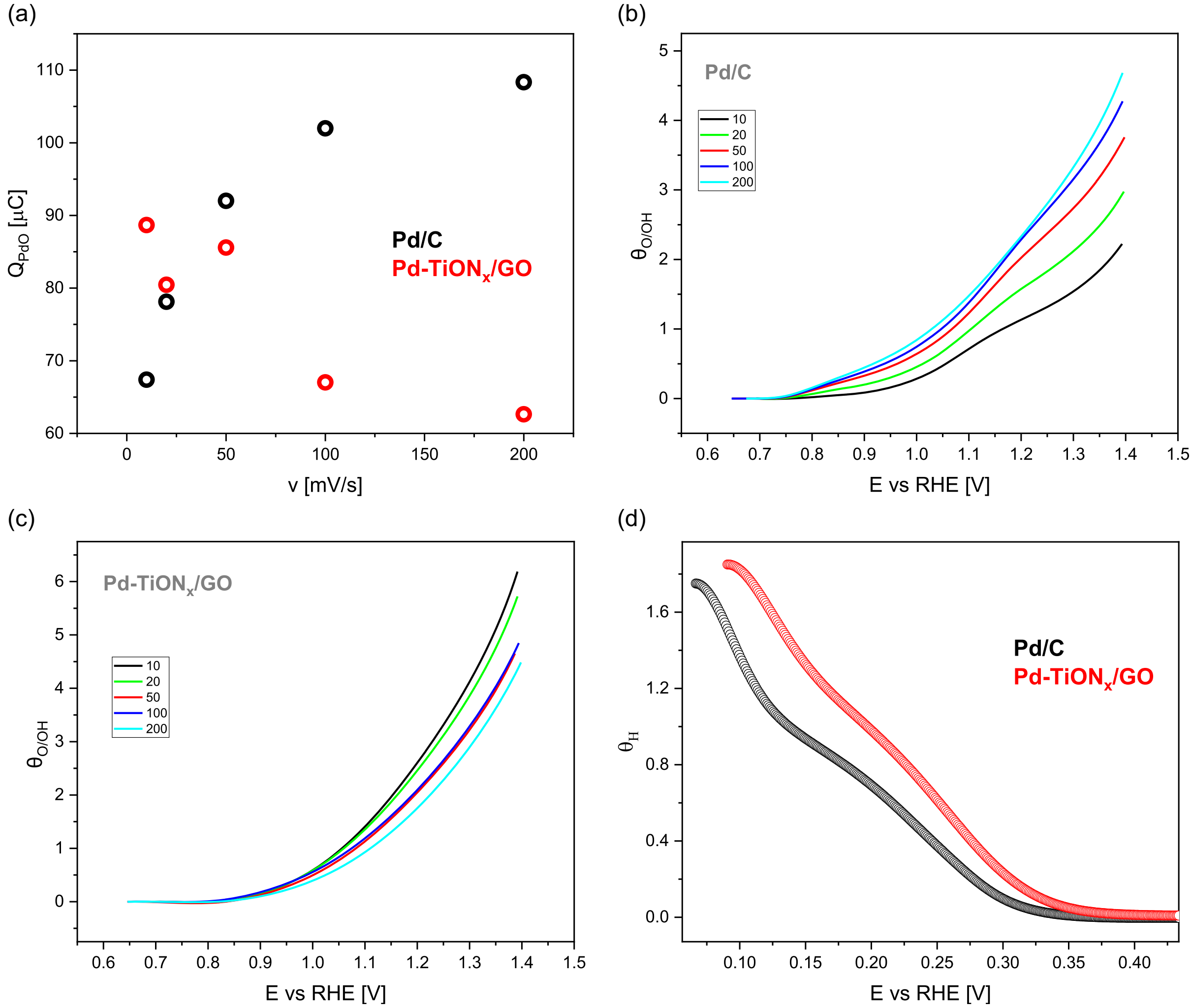

Figure 3. a) Q_{PdO} dependence on the scan rate (v). b) Surface coverage with oxygenated adsorbates ($\theta_{O/OH}$) obtained under different scan rates (mV s^{-1}) for the case of Pd/C and c) Pd-TiON$_x$/GO. d) Surface coverage with adsorbed hydrogen (θ_H, 50 mV s^{-1}).

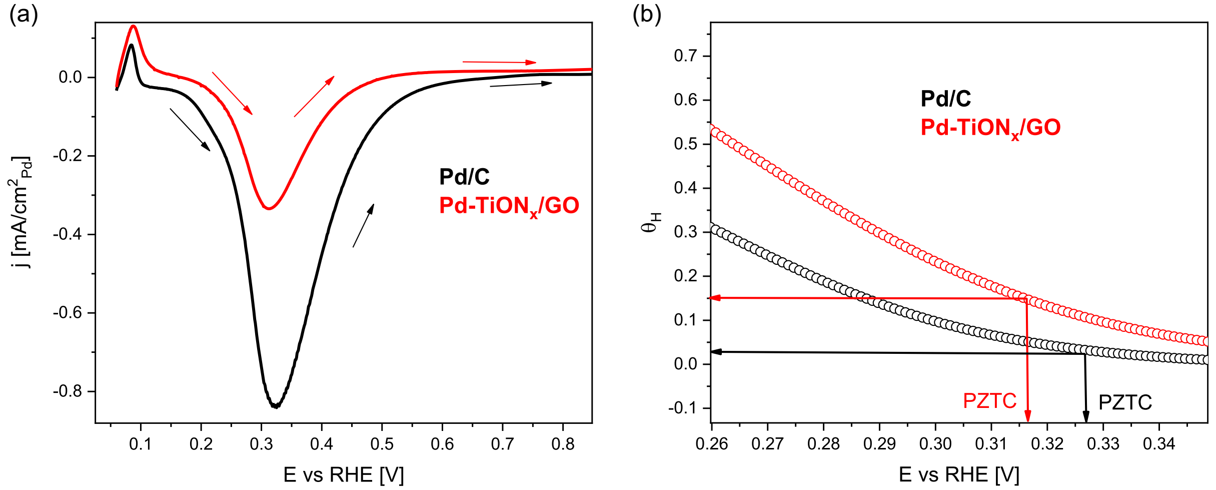

Figure 4. a) N_2O-RR polarization curve normalized per Pd surface area (cathodic scan is shown). b) Surface coverage with adsorbed hydrogen (θ_H, 50 mV s^{-1}) in the potential region of PZTC.

under kinetic control.[64] We exclude the potential effect of the catalyst layer thickness on N_2O-RR since similar catalyst loading was used for the two analogues. Considering that the maximum N_2O-RR rate coincides with a minimum surface coverage by spectators,[65] then in the case of Pd-$TiON_x$/GO, the Pd surface might be at least partially covered by a surface barrier which is poorly permeable to N_2O. Note that such cases have been reported in the past. In particular, nanoparticles can be passivated with an oxide layer (originating from the oxide-based support) induced by electrochemical perturbation.[66–68] Such layers were reported to be permeable to H^+ and impermeable to gases (e.g., O_2).

In order to elucidate the presence of the surface barrier, a detailed STEM analysis was conducted herein operating in the so-called identical location mode, identical location scanning transmission electron microscopy (IL-STEM). This enabled the same spots to be examined throughout different stages of the sample treatment. In our particular case, Pd-$TiON_x$/GO was analyzed before and after the electrochemical pretreatment (see Experimental Section for the details of the protocol). Pd nanoparticles underwent reshaping, with some merging into larger particles due to agglomeration, as seen in **Figure 5**b (and Figure S9, Supporting Information). In contrast, $TiON_x$ didn't exhibit any major transformations, though certain regions showed signs of change near the surface or grain boundaries. The robustness of $TiON_x$ under an acidic regime is in line with our recent studies, which disclose high tolerance toward electrochemical dissolution in 0.1 M $HClO_4$.[69–71] More importantly, overall, the IL-STEM analysis omits the presence of any kind of surface barrier on Pd particles. This highlights that $j_{N2O\text{-}RRmax}$ for the two analogs predominantly depends on θ_H, where θ_H (i.e., N_2O-RR spectator, see also Section S4 in Supporting Information) under $j_{N2O\text{-}RRmax}$ potential is fourfold larger in the case of Pd-$TiON_x$/GO (Figure 4b).

Overall, the differences in redox behavior are a strong incentive to evaluate the performance of the two analogs in the ECH of FF. In particular, we focused on the two main products expected under acidic conditions and at the Pd surface: FA and 2-MF.[72] Initially, we pursued the ECH with a custom-built electrochemical flow cell in which the downstream electrolyte was collected and then analyzed by high-performance liquid hromatography (HPLC) diagnostics. Only FA was detected, as the concentration of 2-MF was most likely below the detection limit, in addition to its unfavorable UV–vis absorption. This is expected as 2-MF is highly volatile (according to Henry's law, solubility constant $H^{cp}{}_s$ values 15000 more volatile than 2-FA at 25 °C).[73] Furthermore, one can expect the 2-MF concentrations to be much lower from FA since the latter is the predominant product under acidic conditions on Pd.[72] Therefore, in order to monitor 2-MF (as well as H_2), electrochemical mass spectrometry (EC-MS) diagnostics were employed, enabling highly sensitive in situ quantification

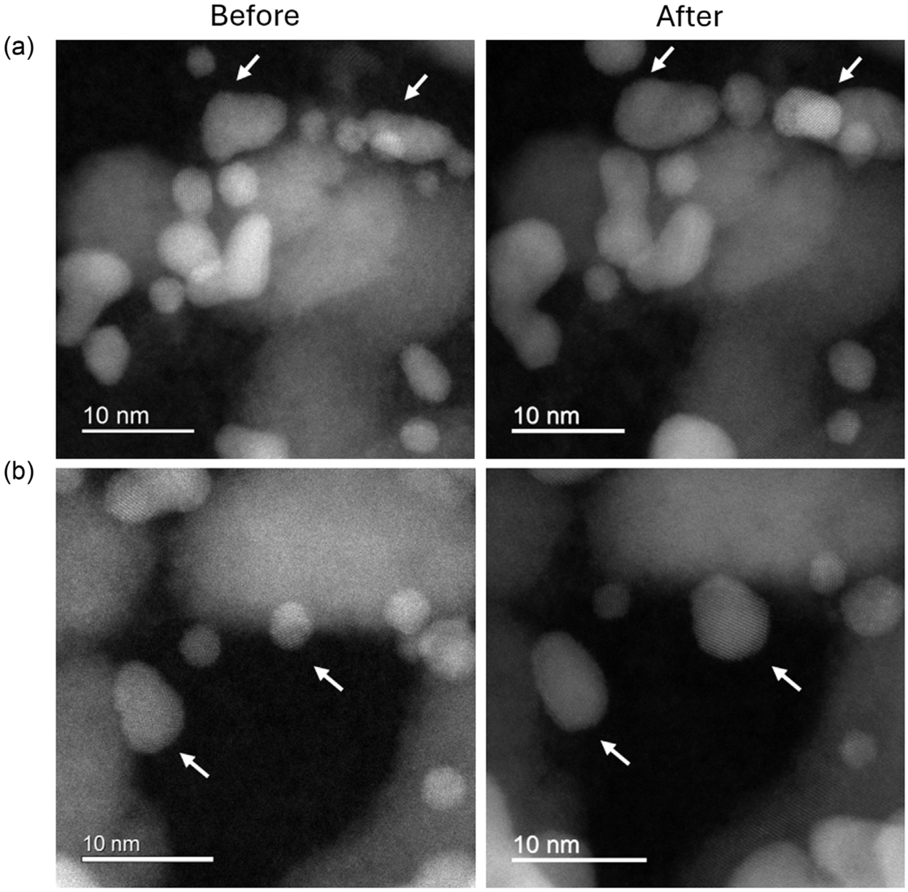

Figure 5. IL-STEM ADF images of Pd-$TiON_x$/GO taken on two different locations: a) and b) illustrating the effect of before and after electrochemical pretreatment and the generation of larger particles, some of them reshaping and merging.

of volatile compounds. This further allows decoupling the partial current densities for an individual product based on calculating the Faradaic current from the MS signal (see SI Section S6).

According to the HPLC analysis, the Pd/C analog shows an approximately twofold higher activity to FA (j_{FA}) within the entire potential window (**Figure 6**a). Interestingly, an opposite trend is seen with respect to $j_{2\text{-}MF}$, where Pd-TiON$_x$/GO is up to 800-fold more active (at 0.05 V, Figure 6b). Similarly, Pd-TiON$_x$/GO is more active toward the competitive hydrogen evolution reaction (HER) (j_{H2}, Figure 6c). Note that the selectivity as well as activity are susceptible to Pd loading,[72] hence similar loadings were used herein for the two analogues. HER can be exploited as a surface probe to explain the ECH trends. In particular, HER is generally strongly inhibited in the presence of strongly adsorbing FF, which reduces the number of free sites for H$_{ads}$ (θ_H).[17,43,74] In this regard, the HER trend for the two analogs implies a lower θ_{FF} (and therefore θ_{FA}) and a higher θ_H for Pd-TiON$_x$/GO compared to Pd/C. Note that this is further supported by the trend in selectivity toward H$_2$, which is two to fourfold higher on Pd-TiON$_x$/GO (Figure 6d), and the analysis of apparent surface coverage of θ_H (Figure 3d). A consequence of the higher θ_H for Pd-TiON$_x$/GO is that j_{FA} is inhibited (Figure 6a). We further emphasize that θ_{FF} (θ_{FA}) is indirectly related to $j_{2\text{-}MF}$. As recently reported in the Pd surface case, FA is a precursor of 2-MF, and at the same time, $j_{2\text{-}MF}$ is strongly influenced by θ_{FA}, where FA blocks the Pd surface, inhibiting $j_{2\text{-}MF}$.[72] Considering that θ_{FA} and θ_{FF} are in a scaling relationship,[75] a higher $j_{2\text{-}MF}$ is obtained for Pd-TiON$_x$/GO. In regards to H$_{ads}$, recent studies highlight the importance of increasing the θ_H for enhancing the 2-MF formation (i.e., a four-proton consuming reaction).[19] Note again that indeed, θ_H is determined to be higher for the Pd-TiON$_x$/GO analog (Figure 3d).

3. Conclusion

The present work demonstrates the influence of TiON$_x$ support material in the redox behavior of palladium nanoparticles (Pd-TiON$_x$/GO) and its consequences for ECH of furfural via a comparative analysis to commercial Pd/C analog under acidic regime. In general, our results reveal an altered electrosorptive behavior due to Pd-TiON$_x$ SMSI. Specifically, voltammetric comparison highlights a distinct shift in the PdO reduction peak, indicating a less oxophilic character for the Pd-TiON$_x$/GO analog. Furthermore, Pd-TiON$_x$/GO exhibits a higher coverage with adsorbed hydrogen and

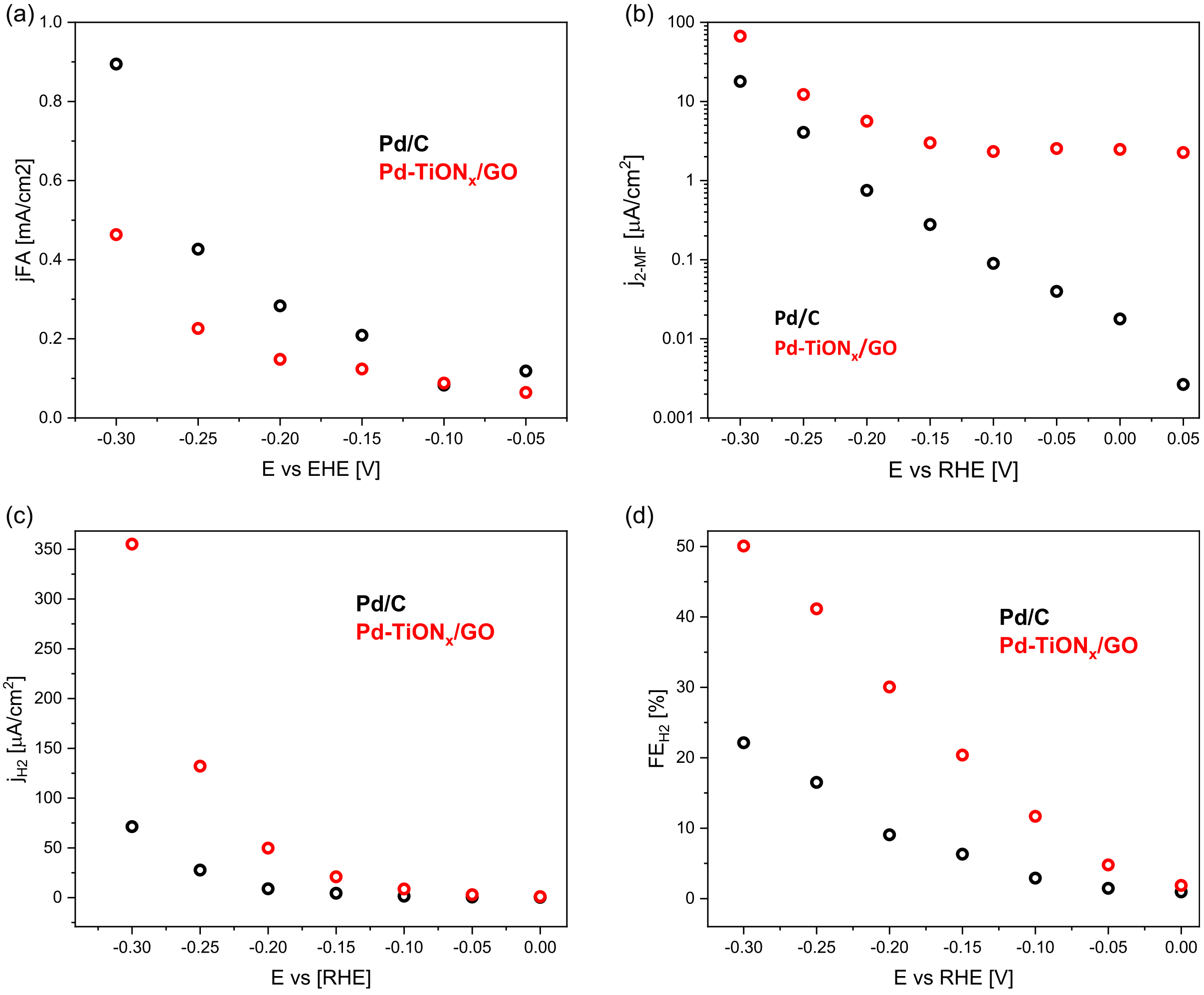

Figure 6. Results of FF reduction under chronoamperometric biasing. a) Partial current densities toward FA formation quantified via HPLC analysis. b) Partial current densities toward 2-MF formation and c) H$_2$ evolution quantified via EC-MS analysis. d) Faradaic efficiencies toward H$_2$.

a more negative value of the PZTC. Overall, distinctive electrosorptive properties have a significant influence on the hydrogenation of furfural. In particular, Pd-TiON$_x$/GO selectivity toward FA is lower than that of Pd/C. In contrast, according to time-resolved probing via the EC-MS diagnostics, a several-fold larger activity for 2-MF (i.e., higher-value product) is obtained for the Pd-TiON$_x$/GO analog. These findings underscore the influence of the support material on Pd's catalytic behavior and provide a promising strategy for optimizing Pd-based catalysts for electrochemical hydrogenation reactions.

4. Experimental Section

Overall, a commercial nanoparticulate catalyst 20 wt% Pd on carbon (Pd/C, Premetek) and a home-made nanoparticulate Pd dispersed on titanium oxynitride were comparatively analyzed.

Synthesis of Pd-TiONx/GO

Graphene oxide (GO) was produced through a modified Hummers' method, as previously documented.[35] In a 5 L beaker, a mixture of 1000 mL of 96 wt% sulfuric acid and 110 mL of 85 wt% phosphoric acid was prepared. Graphite (Imerys) was introduced, and $KMnO_4$ was incrementally added every 24 h, reaching a total of 5 wt eq. After two days of continuous stirring, the reaction was quenched with ice, followed by the addition of 30 wt% H_2O_2 until the color transitioned from purple to yellow. The resulting GO settled overnight, and the supernatant was replaced with ultrapure water. Further purification steps included dispersion in 5 wt% HCl, centrifugation, and re-dispersion in ultrapure water through multiple cycles. The final GO suspension underwent treatment with a homogenizer for 1 h in an ice bath to exfoliate the product. In the next step, amorphous TiO_2 coating on GO was prepared. 2 g of GO was added to a mixture of 0.24 mol of 2-propanol (Honeywell, puriss, p. a.) and 0.02 mol of titanium isopropoxide (Sigma–Aldrich, 97%). After a thorough mixing in a mortar, titanium isopropoxide was hydrolyzed by the addition of 0.8 mol (14.40 mL) of ultrapure water (resistivity 18.2 MΩ cm, MilliQ). The whole mixture was thoroughly mixed and freeze-dried to obtain the dry product. The nitridation of the TiO_2/GO composite was performed by temperature-programmed annealing in NH_3 atmosphere (flow rate was 100 mL min^{-1}). In the first step, temperature was increased at a rate of 2 to 250 °C min^{-1} for 1 h. Next, the temperature was elevated at a rate of 10 to 760 °C min^{-1} for 16 h, and then cooled to room temperature at a rate of 10 °C min^{-1}. Finally, Pd nanoparticles were deposited on the surface of TiON$_x$/GO composite by a modified method described elsewhere.[36] In a typical procedure, 0.1 g of TiON$_x$/GO was ultrasonicated in 10 mL of ultrapure water (MilliQ) for 20 min. To this suspension, 0.0015 mol of polyvinylpyrrolidone (Sigma–Aldrich, mol. wt. 40000) and 0.0009 mol of ascorbic acid (Sigma–Aldrich, 99%) were added, and the whole suspension was stirred on a magnetic stirrer at 80 °C for 10 min. 0.0002 mol of $Pd(NO3)_2\ xH_2O$ (Sigma–Aldrich, 37%–42% Pd) was dissolved in 3 mL of water and quickly added to the heated mixture. The reaction was left under these conditions for 3 h. After, the product was centrifuged at 9000 rpm and washed with water several times. The final product was obtained by freeze-drying.

Structural Characterization/XRD

XRD pattern was recorded using a D4 Endeavor, Bruker AXS diffractometer with Cu-Kα radiation ($\lambda = 1.5406$ Å), and a Sol-X energy-dispersive detector. A step of 0.034° and a holding time of 100 s were used during XRD acquisition.

Structural Characterization/TEM

For the detailed microstructural investigation, a Cs probe corrected STEM (Jeol ARM 200 CF) with an attached Jeol Centurio EDXS system with 100 mm^2 SDD detector and Gatan Quantum ER Dual EELS system was used. IL-STEM of Pd-TiON$_x$/GO sample was carried out by imaging with annular dark field (ADF) and bright field detectors. The sample was prepared by drop-casting an ink of the catalyst on a gold TEM grid (Agar Scientific, Holey Carbon Films on 300 Mesh Gold). In the first step, IL-STEM analysis was performed on the as-prepared grid. In the subsequent step, the prepared grid was assembled into a modified floating apparatus, in detail described in our previous publications.[37,38] The grid was then used as a working electrode under electrochemical perturbation of 100 CVs (0.05–1.2 V, 300 mV s^{-1}) and analyzed under IL-STEM mode again.

Structural Characterization/SEM-EDS

SEM micrographs were obtained using a scanning electron microscope (FE-SEM Zeiss SUPRA 35VP) with an accelerating voltage of 3 or 5 keV and an InLens detector.

Rotating Disc Electrode Measurement

Experiments were carried out using a glassy carbon (GC) rotating disc electrode (Pine, $d = 5$ mm, RDE) in a standard three-compartment cell. The reference electrode used was a reversible hydrogen electrode (RHE) (Gaskatel HydroFlex), and a graphite rod as the counter electrode. Before applying the catalyst ink to the GC same procedure as in other electrochemical measurements was performed. The GC electrode was polished on a 0.5 μm polishing slurry on a TriDent Polishing Cloth (Buehler, USA) prior to the application of the catalyst suspension. Before being applied to the GC electrodes, the suspensions were sonicated for 20 min. For a description of the catalyst suspensions, see section *Electrochemistry coupled with mass spectrometry*. All experiments were performed in 0.1 M $HClO_4$ (prepared from 70% Rotipuran Supra $HClO_4$, Carl Roth) and in the presence of 50 mM FF (Sigma–Aldrich) where specified. All electrochemical measurements were performed using a Biologic SP-300 potentiostat. Initially, both samples underwent an electrochemical pretreatment protocol (100 cycles) between 0.05 and 1.2 V in an Ar-purged electrolyte (300 mV s^{-1}).

Determination of the Electrochemically Active Surface Area (Pd$_{ECSA}$)

Pd$_{ECSA}$ was calculated based on hydrogen under potential deposition charge (Q$_{HUPD}$). The latter was determined via deconvolution due to the overlapping HUPD and Pd hydride (PdH) redox features. Initially, the deconvolution was performed by subtracting the capacitive current. Then HUPD and PdH were deconvoluted using the built-in "multiple peak fit" function in OriginLab, using a Lorentzian function as the fitting function. In the case of Pd/C, the best results were obtained when the HUPD peak was treated as two separate peaks, whereas for Pd-TiON$_x$/GO, the HUPD peak could be treated as a single peak. The fitted peaks were then plotted and integrated using a constant baseline of $y = 0$. Q$_{HUPD}$ was determined at different scan rates (10, 20, 50, 100, 200 mV s^{-1}), and Pd$_{ECSA}$ was calculated from an average of Q$_{HUPD}$ values.

Voltammetry/Apparent Surface Coverage Analysis

Voltammetric experiments were performed via cyclic voltammetry measurements at varied scan rates (10, 20, 50, 100, and 200 mV s^{-1} under Ar-saturated atmosphere, 5 cycles were performed for each respective scan rate), from which the apparent surface coverage was determined as follows. Apparent surface coverage for the two analogs was determined based on differential coefficients of electrochemical adsorption isotherm, defined as $I(E)/v$ (v is the sweep rate, i.e., dE/dt), as a function of applied potential.[39] The integral form, i.e., integrated charge curves (Equation (1)), obtained under different scan rates were used herein.[40] Prior to integration, the curves were corrected for the background current from the double-layer capacitance. The apparent surface coverage (θ) was evaluated using Equation (1) and by calculating Q/Q_{HUPD}. Q_{HUPD} corresponds to a monolayer Pd surface coverage and was determined as an average value from different scan rates (10, 20, 50, 100, 200 mV s^{-1}). An analog coverage analysis was performed to obtain the coverage with hydrogen (θ_H).

$$Q = \int_{E1}^{E2} \frac{I}{v} dE \tag{1}$$

N_2O Reduction Reaction Measurements (N_2O-RR)

N_2O-RR polarization curves were measured in the potential region of 0.05–1.0 V vs RHE (10 mV s^{-1}, 1600 RPM, 0.1 M $HClO_4$). The resistance between the WE and RE was determined using an electrochemical impedance spectroscopy scan and was subsequently compensated (85%) during all measurements via positive feedback.

Electrochemistry Coupled with Mass Spectrometry

EC-MS experiments were performed with the SpectroInlets EC-MS system. The makeup gas used in measurements was 5.0 Helium (Messer). After each measurement, a calibration of the MS detector was performed. The calibration protocol comprised a sequence of galvanostatic pulses (75, 50, 40, 30, 20, 10, 5 μA), 2 min each, where a polycrystalline platinum disc (Pine, $d = 5$ mm) was used as the working electrode. The reference electrode used was a RHE (Gaskatel HydroFlex), and a coiled Pt wire was used as the counter electrode. In between pulses, a rest period of 10 min under controlled potential (0.1 V vs RHE) was imposed to ensure the MS signal for hydrogen returned to baseline. Afterwards, a calibration curve was made by comparing the electrochemical charge obtained from the pulse with the integrated area of the MS signal for hydrogen. A separate calibration was also performed in which a gas mixture containing 1% hydrogen in argon was used as a makeup gas. ECH experiments were performed in 50 mM FF (Sigma–Aldrich) in 0.1 M $HClO_4$ using potentiostatic pulses. These were chosen in the range between 0.2 and −0.35 V (vs RHE), or as negative as possible, keeping in mind the limit of the setup (more than 100 μA of constant H_2 production results in bubbles that significantly interfere with the measurement).[41,42] Pulses lasted for 2 min with a rest period after each pulse to ensure the monitored MS signals returned to the baseline. In the case of 2-MF quantification, the same calibration protocol as described in detail in our previous publication was followed.[43] Catalyst films were prepared by drop-casting 10 μL of freshly sonicated catalyst suspension onto a glassy carbon disc ($d = 5$ mm). The disc was left to dry completely before use. The catalyst suspensions used were prepared by adding 5 mg of catalyst powder to 3 mL of solvent (75% Isopropanol, 25% ultrapure water). After a brief sonication, 65 μL of 5 wt% Nafion solution was added, and the suspension was sonicated until a stable suspension was formed.

Electrochemical Flow Cell Experiments

A custom-made electrochemical cell flow was used for experiments where FA was pursued as the product. The cell encompassed a glassy carbon disk ($d = 5$ mm) as WE. The RE and the CE were separated from the working compartment by glass frits (see Figure S4, Supporting Information). The flow of electrolyte was established using a syringe pump with a flow rate of 20 mL h^{-1}. The electrolyte used was 50 mM furfural in 0.1 M $HClO_4$ (prepared from 70% Rotipuran Supra $HClO_4$, Carl Roth).

HPLC Analysis

HPLC-UV/VIS analysis was performed on an UltiMate 3000 UHPLC system (Thermo Scientific, U.S.A.). Methanol (Chromasolv LC-MS grade, Fluka, Switzerland) and water purified on a MilliQ system from Millipore (Bedford, MA, USA) were used for the preparation of mobile phases, and formic acid from Fluka (p.a. grade purity) was used as modifier. An analytical EC HPLC column Nucleodur C18 HTec (2.0 × 150 mm, 3 μm particle size, Macherey–Nagel) was used with the flow rate of 0.3 mL min^{-1} (the details on the method gradient are given in Supporting Information, Section S5). A mobile phase consisting of acetonitrile and water, both with 0.1% formic acid, was used throughout the work. Injection volume and column temperature were 10 μL and 30 °C, respectively.

Acknowledgements

The authors would like to acknowledge the Slovenian Research and Innovation Agency (ARIS) programs P2-0393, P1-0034, and I0-0003; the projects N2-0155, N2-0337, J7-50227, J2-60043, and MN-0007-104.

Conflict of Interest

The authors declare no conflict of interest.

Data Availability Statement

The data that support the findings of this study are available from the corresponding author upon reasonable request.

Keywords: electrochemical hydrogenations · furfurals · metal–support interactions · nanoparticles · palladium

[1] D. M. Alonso, J. Q. Bond, J. A. Dumesic, *Green Chem.* **2010**, *12*, 1493.
[2] A. Corma Canos, S. Iborra, A. Velty, *Chem. Rev.* **2007**, *107*, 2411.
[3] S. A. Akhade, N. Singh, O. Y. Gutierrez, J. Lopez-Ruiz, H. Wang, J. D. Holladay, Y. Liu, A. Karkamkar, R. S. Weber, A. B. Padmaperuma, M. S. Lee, G. A. Whyatt, M. Elliott, J. L. Male, J. E. Holladay, J. A. Lercher, R. Rousseau, V. A. Glezakou, *Chem. Rev.* **2020**, *120*, 11370.
[4] B. R. Caes, R. E. Teixeira, K. G. Knapp, R. T. Raines, *ACS Sustain. Chem. Eng.* **2015**, *3*, 2591.
[5] X. Li, P. Jia, T. Wang, *ACS Catal.* **2016**, *6*, 7621.
[6] R. Mariscal, P. Maireles-Torres, M. Ojeda, I. Sádaba, M. López Granados, *Energy Environ. Sci.* **2016**, *9*, 1144.
[7] A. Bohre, S. Dutta, B. Saha, M. M. Abu-Omar, *ACS Sustain. Chem. Eng.* **2015**, *3*, 1263.
[8] P. Nilges, U. Schröder, *Energy Environ. Sci.* **2013**, *6*, 2925.
[9] Y. Kwon, K. J. P. Schouten, J. C. Van Der Waal, E. De Jong, M. T. M. Koper, *ACS Catal.* **2016**, *6*, 6704.
[10] A. S. May, E. J. Biddinger, *ACS Catal.* **2020**, *10*, 3212.
[11] S. Jung, E. J. Biddinger, *ACS Sustain. Chem. Eng.* **2016**, *4*, 6500.
[12] T. Lenk, S. Rabet, M. Sprick, G. Raabe, U. Schröder, *ChemPhysChem* **2023**, *24*, e202200614.
[13] X. H. Chadderdon, D. J. Chadderdon, J. E. Matthiesen, Y. Qiu, J. M. Carraher, J. P. Tessonnier, W. Li, *J. Am. Chem. Soc.* **2017**, *139*, 14120.
[14] A. S. May, S. M. Watt, E. J. Biddinger, *React. Chem. Eng.* **2021**, *6*, 2075.

[15] S. Liu, Z. Mukadam, S. B. Scott, S. C. Sarma, M.-M. Titirici, K. Chan, N. Govindarajan, I. E. L. Stephens, G. Kastlunger, *EES Catal.* **2023**, *1*, 539.

[16] L. Zhou, Y. Li, Y. Lu, S. Wang, Y. Zou, *Chinese J. Catal.* **2022**, *43*, 3142.

[17] I. K. M. Yu, F. Deng, X. Chen, G. Cheng, Y. Liu, W. Zhang, J. A. Lercher, *Nat. Commun.* **2022**, *13*, 4.

[18] M. D. Stankovic, J. F. Sperryn, R. S. Delima, C. C. Rupnow, M. B. Rooney, M. Stolar, C. P. Berlinguette, *Energy Environ. Sci.* **2023**, *16*, 3453.

[19] P. Zhou, L. Li, V. S. S. Mosali, Y. Chen, P. Luan, Q. Gu, D. R. Turner, L. Huang, J. Zhang, *Angew. Chemie Int. Ed.* **2022**, *61*, e202117809.

[20] X. Chang, A. F. Liu, B. Cai, J. Y. Luo, H. Pan, Y. B. Huang, *ChemSusChem* **2016**, *9*, 3330.

[21] K. Ji, M. Xu, S. M. Xu, Y. Wang, R. Ge, X. Hu, X. Sun, H. Duan, *Angew. Chemie - Int. Ed.* **2022**, *61*, e202209849.

[22] J. Greeley, I. E. L. Stephens, a S. Bondarenko, T. P. Johansson, H. A. Hansen, T. F. Jaramillo, J. Rossmeisl, I. Chorkendorff, J. K. Nørskov, *Nat. Chem.* **2009**, *1*, 552.

[23] V. R. Stamenkovic, B. Fowler, B. S. Mun, G. Wang, P. N. Ross, C. A. Lucas, N. M. Markovic, *Science* **2007**, *315*, 493.

[24] P. Strasser, S. Koh, T. Anniyev, J. Greeley, K. More, C. Yu, Z. Liu, S. Kaya, D. Nordlund, H. Ogasawara, M. F. Toney, A. Nilsson, *Nat. Chem.* **2010**, *2*, 454.

[25] V. S. Murthi, R. C. Urian, S. Mukerjee, *J. Phys. Chem. B* **2004**, *108*, 11011.

[26] S. J. Tauster, S. C. Fung, R. L. Garten, *J. Am. Chem. Soc.* **1978**, *100*, 170.

[27] G. Fraga, M. S. Santos, M. Konarova, M. D. Hasan, B. Laycock, N. Batalha, S. Pratt, *ChemCatChem* **2021**, *13*, 5191.

[28] J. C. Matsubu, S. Zhang, L. DeRita, N. S. Marinkovic, J. G. Chen, G. W. Graham, X. Pan, P. Christopher, *Nat. Chem.* **2017**, *9*, 120.

[29] I. C. Gerber, P. Serp, *Chem. Rev.* **2020**, *120*, 1250.

[30] M. Haruta, *Catal. Surv. from Japan* **1997**, *1*, 61.

[31] J. J. Pietron, R. M. Stroud, D. R. Rolison, *Nano Lett.* **2002**, *2*, 545.

[32] L. M. Molina, M. D. Rasmussen, B. Hammer, *J. Chem. Phys.* **2004**, *120*, 7673.

[33] M. S. Chen, D. W. Goodman, *Science* **2004**, *306*, 252.

[34] H. Temperature, C. Processes, *Adsorpt. J. Int. Adsorpt. Soc.* **1988**, *119*, 106.

[35] D. C. Marcano, D. V. Kosynkin, J. M. Berlin, A. Sinitskii, Z. Sun, A. Slesarev, L. B. Alemany, W. Lu, J. M. Tour, *ACS Nano* **2010**, *4*, 4806.

[36] R. Long, Y. Li, Y. Liu, S. Chen, X. Zheng, C. Gao, C. He, N. Chen, Z. Qi, L. Song, J. Jiang, J. Zhu, Y. Xiong, *J. Am. Chem. Soc.* **2017**, *139*, 4486.

[37] A. Hrnjić, F. Ruiz-Zepeda, M. Gaberšček, M. Bele, L. Suhadolnik, N. Hodnik, P. Jovanovič, *J. Electrochem. Soc.* **2020**, *167*, 166501.

[38] A. Hrnjic, A. R. Kamšek, A. Pavlišič, M. Šala, M. Bele, L. Moriau, M. Gatalo, F. Ruiz-Zepeda, P. Jovanovič, N. Hodnik, *Electrochim. Acta* **2021**, *388*, 138513.

[39] B. E. Conway, *Prog. Surf. Sci.* **1995**, *49*, 331.

[40] I. A. Pasti, N. M. Gavrilov, S. V. Mentus, *Int. J. Electrochem. Sci.* **2012**, *7*, 11076.

[41] D. Bøndergaard, **2017**.

[42] S. B. Scott, *Ph.D. Thesis*, Isotope-Labeling Studies in Electrocatalysis for Renewable Energy Conversion, and the Net Carbon Impact of This PhD Project, **2019**.

[43] N. Maselj, V. Jovanovski, F. Ruiz-Zepeda, M. Finšgar, T. Klemenčič, J. Trputec, A. R. Kamšek, M. Bele, N. Hodnik, P. Jovanovič, *Energy Technol.* **2023**, *11*, 2201467.

[44] M. Smiljanić, M. Bele, L. Moriau, F. Ruiz-Zepeda, M. Šala, N. Hodnik, *J. Phys. Chem. C* **2021**, *125*, 27534.

[45] M. Grdeń, M. Łukaszewski, G. Jerkiewicz, A. Czerwiński, *Electrochim. Acta* **2008**, *53*, 7583.

[46] L. D. Burke, M. B. C. Roche, *J. Electroanal. Chem.* **1985**, *186*, 139.

[47] V. I. Birss, M. Chan, T. Phan, P. Vanýsek, A. Zhang, *J. Chem. Soc. - Faraday Trans.* **1996**, *92*, 4041.

[48] K. Gossner, E. Mizera, *J. Electroanal. Chem. Interfacial Electrochem.* **1981**, *125*, 347.

[49] A. N. Correia, L. H. Mascaro, S. A. S. Machado, L. A. Avaca, *Electrochim. Acta* **1997**, *42*, 493.

[50] K. Kawasaki, T. Sugita, S. Ebisawa, *J. Chem. Phys.* **1966**, *44*, 2313.

[51] A. Zalineeva, S. Baranton, C. Coutanceau, G. Jerkiewicz, *Langmuir* **2015**, *31*, 1605.

[52] A. Rose, S. Maniguet, R. J. Mathew, C. Slater, J. Yao, A. E. Russell, *Phys. Chem. Chem. Phys.* **2003**, *5*, 3220.

[53] A. Viola, R. Chattot, V. Martin, G. Tsirlina, J. Nelayah, J. Drnec, F. Maillard, *J. Phys. Chem. C* **2023**, *127*, 17761.

[54] R. Chattot, I. Martens, M. Mirolo, M. Ronovsky, F. Russello, H. Isern, G. Braesch, E. Hornberger, P. Strasser, E. Sibert, M. Chatenet, V. Honkimäki, J. Drnec, *J. Am. Chem. Soc.* **2021**, *143*, 17068.

[55] A. J. Zhang, M. Gaur, V. I. Birss, *J. Electroanal. Chem.* **1995**, *389*, 149.

[56] V. Climent, J. M. Feliu, *J. Solid State Electrochem.* **2011**, *15*, 1297.

[57] L. D. Burke, J. K. Casey, *J. Electrochem. Soc.* **1993**, *140*, 1292.

[58] V. I. Birss, V. H. Beck, A. J. Zhang, P. Vanýsek, *J. Electroanal. Chem.* **1997**, *429*, 175.

[59] N. M. Marković, P. N. Ross, *Surf. Sci. Rep.* **2002**, *45*, 117.

[60] A. N. Frumkin, O. A. Petrii, *Electrochim. Acta* **1975**, *20*, 347.

[61] S. Trassati, *Advances In Electrochemical Science And Engineering*, Wiley-VCH Verlag GmbH, Weinheim, FRG **2001**, *7*.

[62] M. J. Weaver, *Langmuir* **1998**, *14*, 3932.

[63] N. R. Avery, *Surf. Sci.* **1983**, *131*, 501.

[64] H. Ebert, R. Parsons, G. Ritzoulis, T. VanderNoot, *J. Electroanal. Chem.* **1989**, *264*, 181.

[65] G. A. Attard, A. Ahmadi, *J. Electroanal. Chem.* **1995**, *389*, 175.

[66] E. Hornberger, A. Bergmann, H. Schmies, S. Kühl, G. Wang, J. Drnec, D. J. S. Sandbeck, V. Ramani, S. Cherevko, K. J. J. Mayrhofer, P. Strasser, *ACS Catal.* **2018**, *8*, 9675.

[67] B. M. Stühmeier, S. Selve, M. U. M. Patel, T. N. Geppert, H. A. Gasteiger, H. A. El-Sayed, *ACS Appl. Energy Mater.* **2019**, *2*, 5534.

[68] B. J. Hsieh, M. C. Tsai, C. J. Pan, W. N. Su, J. Rick, H. L. Chou, J. F. Lee, B. J. Hwang, *Electrochim. Acta* **2017**, *224*, 452.

[69] L. J. Moriau, M. Bele, A. Vižintin, F. Ruiz-Zepeda, U. Petek, P. Jovanovič, M. Šala, M. Gaberšček, N. Hodnik, *ACS Catal.* **2019**, *9*, 11468.

[70] L. Moriau, G. Koderman Podboršek, A. K. Surca, S. Semsari Parpari, M. Šala, U. Petek, M. Bele, P. Jovanovič, B. Genorio, N. Hodnik, *Adv. Mater. Interfaces* **2021**, *8*, 2100900.

[71] A. Lončar, D. Escalera-López, F. Ruiz-Zepeda, A. Hrnjić, M. Šala, P. Jovanovič, M. Bele, S. Cherevko, N. Hodnik, *ACS Catal.* **2021**, *11*, 12510.

[72] N. Maselj, V. Jovanovski, J. Trputec, M. Šala, K. Mervič, N. Hodnik, P. Jovanovič, *ChemCatChem* **2024**, *17*, e202401474.

[73] R. Sander, *Atmos. Chem. Phys.* **2015**, *15*, 4399.

[74] J. A. Lopez-Ruiz, E. Andrews, S. A. Akhade, M. S. Lee, K. Koh, U. Sanyal, S. F. Yuk, A. J. Karkamkar, M. A. Derewinski, J. Holladay, V. A. Glezakou, R. Rousseau, O. Y. Gutiérrez, J. D. Holladay, *ACS Catal.* **2019**, *9*, 9964.

[75] B. Liu, L. Cheng, L. Curtiss, J. Greeley, *Surf. Sci.* **2014**, *622*, 51.

Manuscript received: March 11, 2025
Revised manuscript received: May 28, 2025
Version of record online: July 28, 2025